

Effective impurity behavior emergent from non-Hermitian proximity effect

Deguang Wu¹, Jiasong Chen¹, Wei Su^{2,3}, Rui Wang^{1,4}  , Baigeng Wang^{1,4}  & D. Y. Xing^{1,4}

Non-Hermitian boundaries commonly take place in many open quantum systems locally coupled to a surrounding environment. Here, we reveal a type of non-Hermitian effect induced by non-Hermitian boundaries, the non-Hermitian proximity effect (NHPE), which describes the penetration of non-Hermiticity from the boundary into the bulk. For gapped quantum systems, the NHPE generates in-gap states with imaginary eigenenergies, termed “imaginary in-gap states”. The imaginary in-gap states are localized at the system boundary and decay into the bulk, analogous to the behaviors of the conventional impurity states. However, in contrast to impurity states, the imaginary in-gap states exhibit distinct dynamical behaviors under time-evolution. Moreover, they are physically manifested as corner modes under open boundaries, as a combined result of the non-Hermitian skin effect (NHSE) and NHPE. These results not only uncover implicit similarities between quantum systems with non-Hermitian boundaries and impurity physics, but also point to intriguing non-Hermitian phenomena broadly relevant to open quantum systems.

¹National Laboratory of Solid State Microstructures and Department of Physics, Nanjing University, Nanjing 210093, China. ²College of Physics and Electronic Engineering, Center for Computational Sciences, Sichuan Normal University, Chengdu 610068, China. ³Beijing Computational Science Research Center, Beijing 100084, China. ⁴Collaborative Innovation Center for Advanced Microstructures, Nanjing 210093, China. ✉email: rwang89@nju.edu.cn

Quantum systems that interact with an environment are ubiquitous in physics. The study of the interaction between such systems and baths is of fundamental interest as it leads to various novel quantum effects^{1,2} and applications³. In open quantum systems, although the system and the bath as a whole are Hermitian, the dynamics of the partial system alone can be described by an effective non-Hermitian model⁴. This has recently aroused enormous interest in uniform non-Hermitian quantum systems, where exotic physics have been found, including novel topological phases^{5–17}, skin effects^{18–29}, enriched classifications^{30–41}, and unusual critical phenomena^{42–44}.

It is, however, important to note that non-Hermiticity in realistic open quantum systems can be non-uniform, and in many cases, is only present at the system boundary. We consider systems interacting with their surrounding environments via short-range couplings across boundaries. The general Hamiltonian reads as $H = H_S + H_E + V_{SE}$, where H_S describes the closed quantum system, H_E captures the environment consisting of a continuum of scattering wavefunctions, and V_{SE} describes the coupling between them, which is short-ranged and restricted to the region around the boundary. The renormalization of a quantum system from the environment via V_{SE} is non-negligible⁴, which formally leads to the effective Hamiltonian as

$$H_{\text{eff}} = H_S + \sum_E V_{SE} \frac{1}{\omega^+ - H_E} V_{SE}^\dagger, \quad (1)$$

where $\omega^+ = \omega + i0^+$ and the second term includes the sum of all the scattering channels in the environment. This term arising from system-bath coupling is clearly non-Hermitian. Importantly, since V_{SE} is restricted in real space around the boundary, the non-Hermitian terms take place only at the boundary. The non-Hermitian boundaries implicit in Eq. (1) are common in open quantum systems. However, their effects have not received enough attention in recent studies. Could new phenomena emerge from the non-Hermitian boundaries, and how the non-Hermitian boundaries would affect the quantum systems and their dynamics? These key questions are yet to be addressed.

In this work, we reveal an effect induced by the non-Hermitian boundary, i.e., the non-Hermitian proximity effect (NHPE). We show that the non-Hermiticity of the boundary can penetrate into the nearby quantum systems with a finite penetration depth, akin to the proximity effect of superconductors^{45–48}. For gapped quantum systems, the NHPE induces “in-gap states” with imaginary eigenenergies, i.e., imaginary in-gap states. The imaginary in-gap states display peaks of the local density of states (LDOS) clearly distinct from that of the bulk states. In addition, the imaginary in-gap states decay into the bulk in a way phenomenologically similar to that of conventional impurity problems^{49–54}, where the localized in-gap states decay into the bath^{54–57}. Despite the similarity, the imaginary in-gap states also exhibit several distinct properties. First, the imaginary in-gap states are generally manifested as corner modes under open boundary conditions (OBCs), due to the combined effect of the NHPE and the non-Hermitian skin effect (NHSE). Second, the NHPE leads to unusual dynamical behaviors of the quantum system. In particular, in the cases where the imaginary part of the imaginary in-gap state eigenenergy is positive, the probability distribution of the imaginary in-gap state keeps increasing due to the gain from the environment. As a result, under time evolution, all wave packets will be evolved into the imaginary in-gap states displayed as corner modes under OBCs. Our work reveals that impurity-like behaviors with unusual dynamics can emerge from quantum models with non-Hermitian boundaries. This points to a new direction that intertwines impurity physics and non-Hermitian effects, which could commonly take place in open quantum systems.

Results

Imaginary in-gap states. We exemplify our study by starting with the Qi-Wu-Zhang (QWZ) model⁵⁸ describing 2D Chern insulators on a square lattice (Fig. 1a), i.e.,

$$H_0 = \sum_{x,y} \left\{ \left[c_{x+1,y}^\dagger \frac{(i\sigma_x - \sigma_z)}{2} c_{x,y} + c_{x,y+1}^\dagger \frac{(i\sigma_y - \sigma_z)}{2} c_{x,y} \right] + c_{x,y}^\dagger m\sigma_z c_{x,y} \right\} + h.c., \quad (2)$$

where $c(x, y) = [c_{a,x,y}, c_{b,x,y}]^T$ is the spinor with a, b sublattice. We further consider the non-Hermitian terms along the boundary $y = 1$:

$$H_y = i \sum_x c_{x,1}^\dagger \gamma \sigma_x c_{x,1}. \quad (3)$$

Eq. (3) describes a non-Hermitian boundary as indicated by the red sites in Fig. 1a, which can be generated by coupling H_0 to an environment at $y = 1$.

We first assume the cylinder geometry, i.e., the periodic boundary condition along x and OBC along y with $y \in [1, L_y]$. The real and imaginary parts of the energy spectrum are numerically obtained and shown in Fig. 1b, c, respectively. Two chiral edge states of the Chern insulator are observed in the real spectrum, connecting the conduction and valence band. These two edge states are respectively localized at the upper ($y = 1$) and lower ($y = L_y$) boundary, as shown by Fig. 1d. It is also shown in Fig. 1c that the upper chiral mode displays nonzero imaginary spectrum while the lower mode remains real. This is expected since the non-Hermitian term γ is only applied on the upper boundary.

Despite the chiral edge states, we also observe two channels of in-gap modes for $-0.6 \lesssim k_x \lesssim 0.6$, as marked by the red solid curves in Fig. 1b. These in-gap modes do not connect the conduction and valence band, suggesting that they have a non-topological physical origin. Both channels describe edge states localized at the upper boundary, as evidenced by Fig. 1d. Moreover, as shown by Fig. 1c, each mode with fixed k_x (marked by a red dot) in the two edge states exhibits nonzero imaginary eigenenergy, thus termed as the imaginary in-gap state. We note that the dispersion of imaginary in-gap states has finite extensions into the bulk states with displaying “tail” states, as marked by the red dashed curves in Fig. 1b.

Non-Hermitian proximity effect. To reveal the origin of imaginary in-gap states, we first perform a real-space renormalization group (RG) analysis (see Supplementary Note 1). We decompose the total system $H = H_0 + H_y$ into a series of coupled 1D horizontal layers, i.e., $H = \sum_{k_x} [\sum_{l=1}^{L_y} H_{l,k_x} + \sum_{l=1}^{L_y-1} H_{l,l+1,k_x}]$, where H_{l,k_x} is the Hamiltonian of the l th layer, and $H_{l,l+1,k_x}$ depicts the coupling between the l th and $(l+1)$ th layer. The non-Hermitian boundary, i.e., Eq. (3), is included in H_{1,k_x} , which reads as, $H_{1,k_x} = (\sin k_x + i\gamma)\sigma_x + (m - \cos k_x)\sigma_z$. Then, we integrate out the $l = 1$ layer and obtain a renormalized Hamiltonian for the rest of the system, whose top layer ($l = 2$) now becomes non-Hermitian. Then, as indicated by Fig. 2a, by iteratively repeating the above procedure, the effective Hamiltonian for the $(l+1)$ th layer can be obtained after the l th RG step as,

$$H_{l+1,k_x}^{\text{eff}} = \sin k_x \sigma_x + (m - \cos k_x) \sigma_z + f_l (\sigma_0 + \sigma_x), \quad (4)$$

where f_l is the complex self-energy with k_x -dependence. In Fig. 2b, we plot the calculated $\text{Im}[f_l]$, as a function of the RG step l . As shown, $\text{Im}[f_l]$ decays with l for all k_x , and saturates to the fixed point $\text{Im}[f_l] = 0$ for large l . This shows that the non-Hermitian terms on the boundary can effectively penetrate into the bulk with a penetration depth. Due to its analogy with the proximity effect

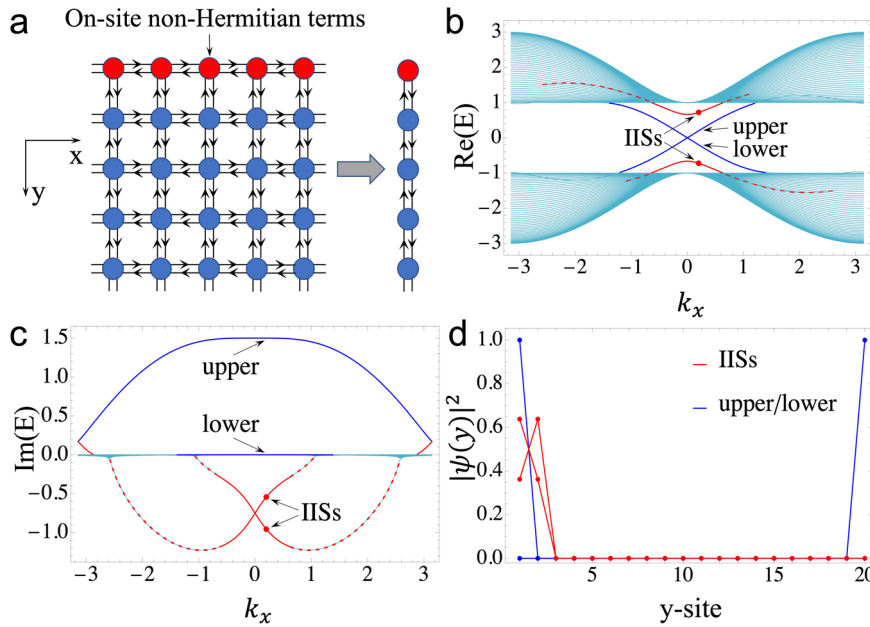


Fig. 1 Imaginary in-gap states (IISs) induced by non-Hermitian boundary. **a** The Qi-Wu-Zhang (QWZ) model with on-site non-Hermitian boundary terms $i\gamma\sigma_x$ (marked by red circles) on the top layer of the system and on-site mass terms $m\sigma_z$ (marked by blue circles). Under the cylinder geometry (the size of the system in the y -direction is denoted by L_y), for any fixed k_x , the model is described by a 1D vertical chain with a non-Hermitian term on its first site. **b, c** The real and imaginary parts of the spectrum for the model $H = H_0 + H_\gamma$ under the cylinder geometry, where H_0 is given by Eq. (2), and H_γ is given by Eq. (3). The imaginary in-gap states expand into the bulk states as “tail” states marked by the red dashed curves. The parameters used are $m = 1.0$, $\gamma = 1.5$ and $L_y = 20$. **d** The probability distribution of the imaginary in-gap states and the topological chiral edge states with $k_x = 0.2$, which are marked by the arrows in (b) and (c).

of superconductivity where Cooper pairs leak into the adjacent system, we term it the NHPE.

To better visualize the NHPE, we adopt OBCs along both x and y directions and calculate the spatial distribution of the eigenstates of H . The typical spatial distribution of the bulk states is shown in Fig. 2c. It is clear that the bulk states remain as Bloch states and are barely affected by the non-Hermitian effects. This is expected from Fig. 2b since the non-Hermitian terms are negligible for bulk states far away from the upper boundary. Then, we focus on the imaginary in-gap states and pick up their corresponding eigenstates under OBCs. The typical spatial distribution of imaginary in-gap states is shown in Fig. 2d, e. Due to the NHSE, which is significant near $y = 1$, the imaginary in-gap states are found to localize either at the right or left boundary, depending on the sign of γ (Fig. 2d, e, respectively). Moreover, they are also localized at the upper boundary due to the NHPE, with a short localization length along y up to a few layers. Therefore, the combination of NHSE and NHPE generally drives the imaginary in-gap states into corner modes under OBCs. In addition, we also plot in Fig. 2f the distribution of the “tail states” (the dashed curve in Fig. 1b) deep in the bulk. Compared to the imaginary in-gap states, these states are found to exhibit longer localization lengths along y because of their smaller imaginary part of eigenenergies.

The analogy between imaginary in-gap states and impurity states. So far, we have shown that the imaginary in-gap states manifest themselves as edge modes and corner modes under the cylinder geometry and OBCs, respectively. For both cases, the imaginary in-gap states are localized at the upper boundary and decay along y , as a result of the NHPE induced by the non-Hermitian boundary.

To further reveal the physical nature of imaginary in-gap states, we now demonstrate their underlying similarity with the conventional impurity states in gapped systems. Under the

cylinder geometry, k_x is a good quantum number. The total system can then be written as $H = \sum_{k_x} H_{k_x}$, and

$$H_{k_x} = \sum_y [c_{k_x, y+1}^\dagger T_y c_{k_x, y} + h.c.] + \sum_y \epsilon_{k_x} c_{k_x, y}^\dagger c_{k_x, y} + ic_{k_x, 1}^\dagger \gamma \sigma_x c_{k_x, 1}, \quad (5)$$

where $c_{k_x, y} = [c_{a, k_x, y}, c_{b, k_x, y}]^T$, $T_y = (i\sigma_y - \sigma_z)/2$ and $\epsilon_{k_x} = [\sin k_x \sigma_x + (m - \cos k_x) \sigma_z]$. For fixed k_x , H_{k_x} describes a 1D vertical chain model with a non-Hermitian term on its first site, as indicated by Fig. 1a. It is clear that the localization and decay behaviors of an imaginary in-gap state are fully captured Eq. (5).

We now calculate the LDOS from Eq. (5). The density of states (DOS) can be obtained from the imaginary part of the retarded Green’s function GF, i.e., $\rho(\epsilon) = -\frac{1}{\pi} \text{ImTr} \left[\sum_n \frac{1}{\epsilon + i0^+ - E_n} \langle \psi_n^R | \psi_n^L \rangle \right]$, where E_n is the n th complex eigenvalues. Here, compared to the Hermitian cases, the support of DOS is expanded to the complex plane^{59,60}, i.e., $\epsilon = \epsilon_r + i\epsilon_i$. Besides, both the left and right eigenstates have been used to form the complete basis⁶¹ that expands the GF. Then, the LDOS at the l -th site of the chain can be derived as $\rho_l(\epsilon_r, \epsilon_i) = \frac{1}{N} \sum_n \delta(\epsilon_r - \text{Re}[E_n]) \delta(\epsilon_i - \text{Im}[E_n]) |\langle \psi_n^R | l \rangle \langle \psi_n^L | l \rangle|$.

We show in Fig. 3a, b the calculated LDOS, with focusing on the imaginary in-gap state region ($-0.6 \lesssim k_x \lesssim 0.6$). At the boundary site $y = 1$ (Fig. 3a) of the 1D vertical chain, except for the topological edge mode from the upper chiral edge state, we observe two significant LDOS peaks located at energies with $\epsilon_i < 0$. These peaks come from the two imaginary in-gap states localized at $y = 1$. Moving away from $y = 1$, the imaginary in-gap state peaks quickly decay. Meanwhile, the LDOS from the bulk states emerges, which is located on the real energy axis. As shown by Fig. 3b, for $y \gg 1$, both the peaks from the imaginary in-gap states and the topological edge state disappear, leaving only the

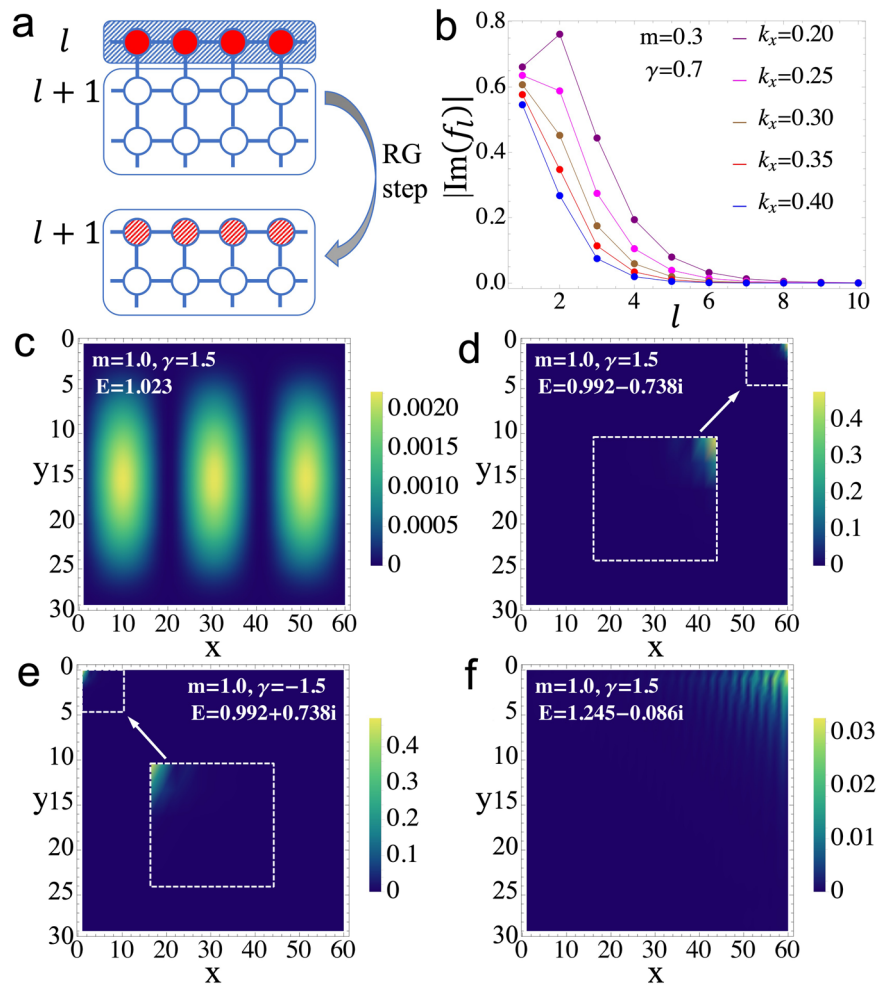


Fig. 2 Non-Hermitian proximity effect and the corner modes under open boundary conditions (OBCs). **a** Schematic plot of the real-space renormalization group (RG) procedure. The renormalized $(l+1)$ th layer can be obtained after integrating out the l th layer. **b** The imaginary part of the complex self-energy f_l as a function of the RG step l for different k_x . $\text{Im}[f_l]$ decays with l and eventually saturates to the fixed point $\text{Im}[f_l] = 0$ for large l . The model we use is $H = H_0 + H_\gamma$, where on-site non-Hermitian boundary terms $i\gamma\sigma_x$ are on the top layer of the system. **c-f** The probability distribution of eigenstates under OBCs with size $L_x \times L_y = 60 \times 30$, the color bars on the right side of the panels indicate its value under normalization. **c** The case for the bulk states. **d, e** are results for the imaginary in-gap states with opposite values of γ , and **f** shows the result for the “tail state” deep in the bulk.

bulk states. The LDOS projected to the real energy axis is also shown in Fig. 3c, d for clarity.

To clearly show the similarity between imaginary in-gap states and impurity states, we consider a non-interacting pseudospin Anderson impurity model coupled to the QWZ model, i.e., $H_{\text{imp}} = H_0 + H_f$, where the impurity is described by

$$H_f = \sum_{\sigma} \epsilon_f f_{\sigma}^{\dagger} f_{\sigma} + V \sum_{\mathbf{k}, \sigma} (f_{\sigma}^{\dagger} c_{\mathbf{k}, \sigma} + h.c.). \quad (6)$$

f_{σ} is the annihilation operator of the impurity state with pseudospin (sublattice) σ , ϵ_f denotes the impurity energy level (independent of σ), and V its hybridization with the bath electrons. Although the impurity considered in Eq. (6) is located in the bulk of the 2D Chern insulator as shown by Fig. 3e, the low-energy impurity state is accurately determined by a 1D Wilson open chain following the numerical renormalization group mapping scheme (see Supplementary Note 4), as schematically shown by Fig. 3e. The Wilson open chain shares a similar structure with the 1D vertical chain model in Fig. 1a. Both of them describe a boundary site ($y = 1$) coupled to bath degrees of freedom ($y > 1$) via the nearest neighbor coupling. It should be noted that the $y > 1$ sites on the Wilson chain represent the bath states in discretized energy windows. The site is closer to the

impurity ($y = 1$) and describes the states in the higher energy window, i.e., in the shorter length scale measured from the impurity.

We then calculate the LDOS on different sites of the Wilson chain, as shown in Fig. 3f, g. For y being close to the impurity, two in-gap states emerge, due to the coupling of the impurity to the conduction and valence band electrons. With tuning y away from the impurity, the LDOS from the impurity states decreases and that from the bulk states increases. For large y , only the LDOS of the low-energy bulk states are left, which are located around the gap energy, as shown in Fig. 3g. The LDOS shown in Fig. 3f, g is qualitatively in analogy with the projected LDOS in Fig. 3c, d, implying the similarity between the imaginary in-gap states and the impurity physics.

Distinct dynamical behaviors of imaginary in-gap states.

Despite the similarity, the imaginary in-gap states also exhibit some distinct features. First, since the LDOS peaks of imaginary in-gap states are located in the complex energy plane with $\epsilon_i \neq 0$, they can persist even if their real parts of eigenenergies are immersed in the bulk continuum (see Supplementary Note 2). This explains the existence of the “tail states” observed in Fig. 1b. Second, the imaginary in-gap states exhibit unusual dynamical

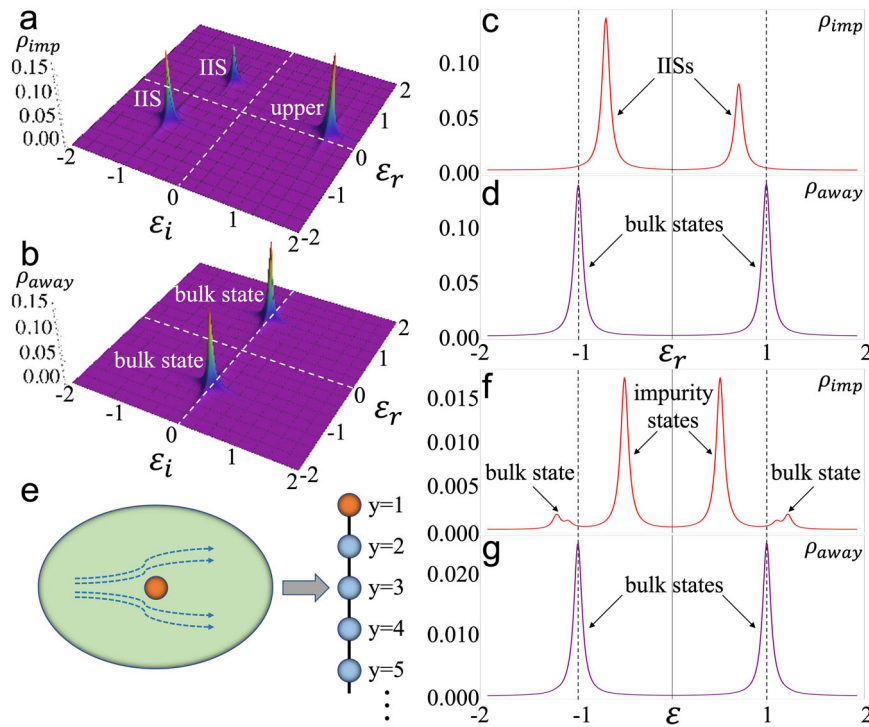


Fig. 3 Analogy between imaginary in-gap states and impurity states and their local density of states (LDOS). **a, b** The LDOS of the non-Hermitian 1D vertical chain model (for fixed k_x) in Eq. (5) with a non-Hermitian term $i\gamma\sigma_x$ on its first site and on-site mass terms $m\sigma_z$. The parameters are $m = 1.0$, $\gamma = 1.5$, and $k_x = 0.2$. In **a**, there emerge two imaginary in-gap state (IIS) peaks together with that from the upper topological edge state at $y = 1$. In **b**, far away from the boundary ($y = 7$), only the LDOS from bulk states is left which is located on the real energy axis. **c, d** The projections of **(a)** and **(b)** onto the real axis. The LDOS from the topological edge state, which is not our focus, has been excluded for clarity. The gap energy is at $\omega = \pm 1$, as marked by the dashed lines. **e** Schematic plot of an impurity embedded in the bath, which is mapped to a 1D Wilson open chain. **f, g** The calculated LDOS of the impurity model with the impurity level ϵ_f and the hybridization V . The parameters used are $m = 1.0$, $\epsilon_f = 0$, and $V = 3.0$. In **f**, two impurity in-gap states emerge near the impurity site, and two minor peaks also arise from the mixing with the bulk states. In **g**, far away from the impurity, only the low-energy bulk states are left in the LDOS.

behaviors absent in the Hermitian systems, as a result of their imaginary eigenenergies. Under time evolution, the amplitude of an imaginary in-gap state either grows or decays, depending on the sign of γ (see Supplementary Note 3). This is a reflection of the non-Hermitian nature of the imaginary in-gap states, in contrast with the conventional impurity states.

For a Gaussian wave packet input at the bottom layer of the system, the time-evolution of the wave packet is calculated under OBCs and shown in Fig. 4a–c (for $\gamma < 0$). The wave packet first diffuses into the bulk (Fig. 4b) and then gradually evolves into the imaginary in-gap state eigenstate localized at the top layer. Due to the NHSE, it finally turns into the corner state as shown in Fig. 4c. We also start from a Gaussian wave packet placed at any generic site at the top layer. As shown by Fig. 4d, the wave packet also evolves into the imaginary in-gap state located at the corner. Hence, we observe that, for $\gamma < 0$ where the amplitude of imaginary in-gap states grows, a generic Gaussian wave packet will always evolve into the cornered imaginary in-gap state (see Supplementary Note 3 for the $\gamma > 0$ case). Such a dynamical feature is a clear distinction between imaginary in-gap states and conventional in-gap states.

Discussion

This work reveals an impurity-like non-Hermitian phenomenon induced by non-Hermitian boundaries. Although the imaginary in-gap state constitutes an edge mode, each individual imaginary in-gap state can be further explored to simulate impurity physics with novel non-Hermitian properties^{62,63}. For example, by

properly introducing Hubbard interaction U on the boundary, the corresponding 1D vertical chain model in Eq. (5) would bare similarities with the Wilson chain mapped from a finite U Anderson model. Hence, Kondo-like behaviors could emerge but be enriched by new features arising from the non-Hermiticity.

Although a non-Hermitian boundary with alternating gain and loss in Eq. (3) is studied as an example, as we show in Methods, the NHPE and the corresponding imaginary in-gap states remain intact for gain-only or loss-only boundaries as well. In addition, we also investigate a more general 2D insulator model with non-Hermitian boundaries. As shown in Methods, although the NHSE is absent in this model, the NHPE still persists, leading to imaginary in-gap states that are manifested by a localized edge mode shown in Fig. 5f (rather than the corner mode in Fig. 2d). The model independence indicates that the NHPE should be a more general non-Hermitian effect than NHSE.

The theoretical model studied here could be realized in different experimental platforms. For example, the Chern insulator model H can be realized by magnetically doped topological insulators⁶⁴. Moreover, the non-Hermitian boundary terms can be realized on the basis of reservoir engineering. The loss or gain on the boundary can be achieved by using a nonlocal coupling to auxiliary degrees of freedom which undergo local loss or gain¹¹, as discussed in detail in Methods. Moreover, the 2D topological insulating phases can also be realized by cold atoms in optical lattices or photons in coupled cavities⁶⁵. In particular, in arrays of coupled micro-ring cavities, the photon gain and loss for each cavity can be controlled independently^{66,67}. These provide

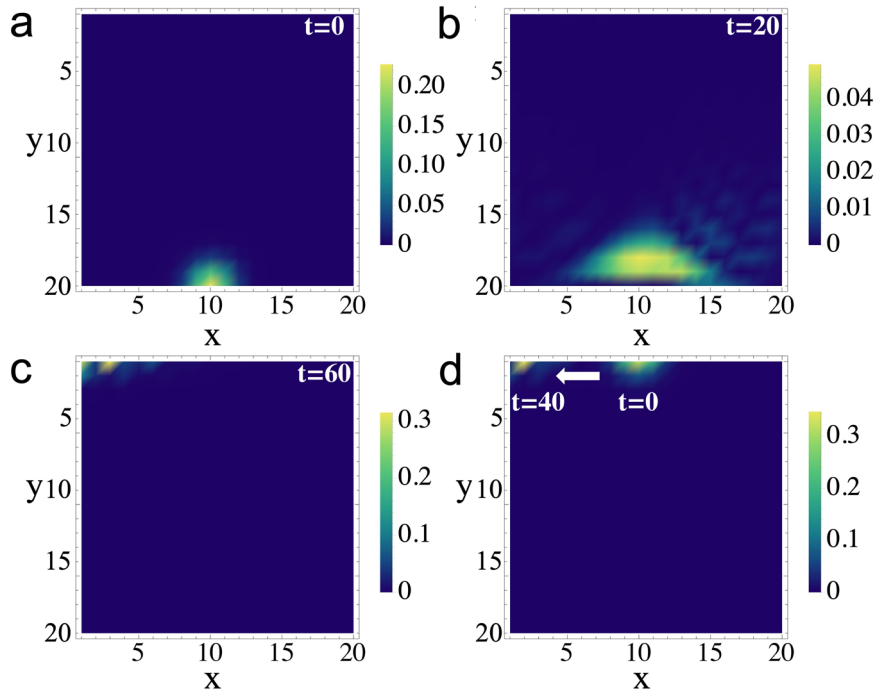


Fig. 4 Time-evolution of the wave packet. **a** The initial state is set to be a Gaussian wave packet, placed at the bottom layer of a square lattice with size $L_x \times L_y = 20 \times 20$. The model is described by $H = H_0 + H_\gamma$, where H_0 is given by Eq. (2) which contains on-site mass terms $m\sigma_z$, and H_γ is given by Eq. (3) with the on-site non-Hermitian boundary terms $i\gamma\sigma_x$ located on the top layer of the system. The wave packet evolves according to the Schrödinger equation. **b** The Gaussian wave packet diffuses into the bulk. **c** The Gaussian wave packet eventually evolves into the imaginary in-gap state localized at the upper-left corner. **d** The evolution of a wave packet initially placed at the top layer. The color bars on the right side of the panels indicate the value of the normalized probability distribution at different times. Common parameters: $m = 1.0$, $\gamma = -1.5$.

promising platforms to further investigate the predicted NHPE, the imaginary in-gap states, as well as their dynamical behaviors.

Methods

Real-space renormalization group analysis of non-Hermitian proximity effect.

For the open boundary perpendicular to the y -direction, the total system of a 2D lattice can be decomposed into a series of horizontal layers (labeled by l) with inter-layer coupling, and its partition function is then cast into

$\mathcal{Z} = \int \prod_l \mathcal{D}\bar{\psi}_l \mathcal{D}\psi_l e^{-(S_l + S_{l+1})}$, where

$$S_l = - \sum_{i\omega_n} \sum_{k_x \in \text{BZ}} \bar{\psi}_{k_x, i\omega_n, l} [i\omega_n - H_l(k_x)] \psi_{k_x, i\omega_n, l}, \quad (7)$$

where $\psi_{k_x, i\omega_n, l} = [c_{a, k_x, i\omega_n}, c_{b, k_x, i\omega_n}]^T$ is the Grassmann field. $H_l(k_x)$ is the Hamiltonian of the l th horizontal chain. The action for the inter-layer coupling can be written as

$$S_{l, l+1} = - \sum_{i\omega_n} \sum_{k_x \in \text{BZ}} (\bar{\psi}_{k_x, i\omega_n, l} T_y \psi_{k_x, i\omega_n, l+1} + h.c.), \quad (8)$$

where T_y is the matrix describing the interlayer hopping, which is assumed to be l -independent. Since the action is bilinear in terms of Grassmann fields, we can integrate out the first layer and obtain a renormalized effective action for the second layer as

$$S_2 = - \sum_{i\omega_n} \sum_{k_x \in \text{BZ}} \bar{\psi}_{k_x, i\omega_n, 2} G_2^{-1}(i\omega_n, k_x) \psi_{k_x, i\omega_n, 2}, \quad (9)$$

where $G_2^{-1}(\omega, k_x) = \omega^+ - H_2(k_x) - T_y^\dagger(\omega^+ - H_1(k_x))^{-1} T_y$ is the renormalized retarded Green's function of the second layer with $\omega^+ = \omega + i0^+$. To extract the low-energy effective Hamiltonian, the low-frequency approximation can be made in $G_2^{-1}(\omega, k_x)$, which well preserves the low-energy physics as long as the layer integrated out remains gapped (which is indeed the case for the QWZ model studied here, where each layer describes a 1D Su-Schrieffer-Heeger (SSH) model). Then, the effective Hamiltonian of the second layer is read off as

$$H_2^{\text{eff}}(k_x) = H_2(k_x) - T_y^\dagger \frac{1}{H_1(k_x)} T_y. \quad (10)$$

By treating the renormalized second layer as the first layer on top of the remaining system, then the above procedure can be performed iteratively, leading to the effective action for the renormalized third, fourth... layers. After l RG steps, an iterative relationship between the effective Hamiltonian of the l th and that of the

$(l+1)$ th layer can be obtained as

$$H_{l+1}^{\text{eff}}(k_x) = H_l(k_x) - T_y^\dagger \frac{1}{H_l^{\text{eff}}(k_x)} T_y. \quad (11)$$

Now we apply the real-space RG transformation to the QWZ model with a non-Hermitian boundary, the first layer Hamiltonian with non-Hermitian terms is given by

$$H_1(k_x) = (\sin k_x + i\gamma)\sigma_x + (m - \cos k_x)\sigma_z, \quad (12)$$

which is a non-Hermitian version of the SSH model and exhibits a non-Hermitian skin effect¹⁸. We then derive the effective Hamiltonian for the renormalized l th layer under the real-space RG transformation. For any 2×2 matrix A , it can be expanded into a linear combination, $A = a\sigma_0 + b\sigma_x + c\sigma_y + d\sigma_z$, where $\sigma_{x,y,z}$ and σ_0 are the Pauli matrices and identity matrix, respectively. Then, we have

$$T_y^\dagger A^{-1} T_y = \frac{a+b}{2\text{Det}[A]} (\sigma_0 + \sigma_x), \quad (13)$$

with $\text{Det}[A] = a^2 - (b^2 + c^2 + d^2)$. Using the Eqs. (10), (12), and (13), we have

$$H_2^{\text{eff}}(k_x) = \sin k_x \sigma_x + (m - \cos k_x) \sigma_z + f_1 (\sigma_0 + \sigma_x), \quad (14)$$

where $f_1 = (\sin k_x + i\gamma)/[2(2 - 2\cos k_x + 2i\gamma \sin k_x - \gamma^2)]$ is the self-energy due to the renormalization of the first layer. Accordingly, we can express the effective Hamiltonian of the $(l+1)$ th layer in the same form as Eq. (14), i.e., Eq. (4). Substituting it into the Eqs. (11) and (13), an iterative relation between f_{l+1} and f_l can be obtained

$$f_{l+1} = \frac{\sin k_x + 2f_l}{2(2 \sin k_x f_l - 2m \cos k_x + m^2 + 1)}. \quad (15)$$

The fixed points, if exist, can be determined by requiring $f_{l+1} = f_l = f_c$ for $l \rightarrow \infty$. This leads to the following equation

$$4 \sin k_x f_c^2 - 2m(2 \cos k_x - m)f_c - \sin k_x = 0. \quad (16)$$

Since $\Delta = 4m^2(2 \cos k_x - m)^2 + 16 \sin k_x^2 \geq 0$, the two roots f_{c1} and f_{c2} of Eq. (16) are given by

$$f_{c1/c2} = \frac{2m(2 \cos k_x - m) \pm \sqrt{\Delta}}{8 \sin k_x}, \quad (17)$$

which implies that the self-energy f_l are real at the fixed points. This explains why the imaginary part of f_l eventually vanishes for large l , as shown in Fig. 2b. In

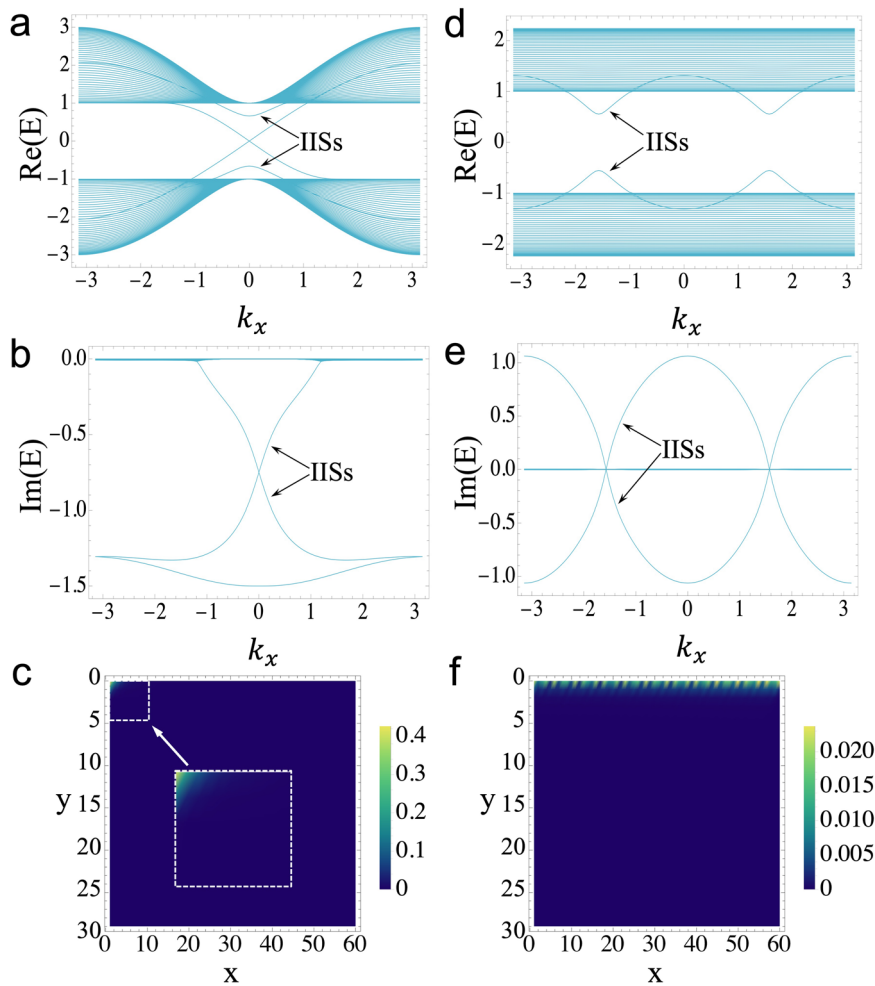


Fig. 5 Generality of the non-Hermitian proximity effect (NHPE). **a, b** The real and imaginary parts of the spectrum for the model $H = H_0 + H_y$, where H_0 is described by Eq. (2) which contains on-site mass terms $m\sigma_z$, and H_y is described by Eq. (18) with the on-site non-Hermitian boundary terms $i\gamma\sigma_0$ located on the top layer of the system. The model obeys cylinder geometry with size in the y -direction being $L_y = 50$. The parameters used are $m = 1.0$ and $\gamma = -1.5$. **c** The probability distribution of the imaginary in-gap states (IISs) with open boundary conditions (OBCs) with size $L_x \times L_y = 60 \times 30$, where the imaginary in-gap state ($E = -0.451 - 1.222i$) is located at the corner due to the combined effects of the NHPE and the non-Hermitian skin effect (NHSE). The color bar on the right side of the panel indicates the value of the probability distribution under normalization. **d-f** Analogous to **a-c**, with H_0 now being described by Eq. (19) and H_y now being described by Eq. (3), where the parameters used are $m = 1.0$ and $\gamma = 1.5$. In **f**, the imaginary in-gap state ($E = 0.746 + 0.464i$) is an edge mode evenly distributed along the upper boundary, since only the NHPE exists in this model.

addition, we can prove that f_l eventually flows to only one of the fixed points f_{c1} . More subtle details can be found in the Supplementary Note 1.

The general existence of NHPE in gapped states with non-Hermitian boundaries. Although the non-Hermitian effects are derived from Eqs. (2) and (3), which describe a Chern insulator with a boundary that has alternating gain and loss (on a and b sites), the NHPE found here is in fact general. To demonstrate its generality, we first consider the non-Hermitian boundaries with only gain or only loss. Hence, we replace Eq. (3) by

$$H_y = i \sum_x c_{x,1}^\dagger \gamma \sigma_0 c_{x,1}, \tag{18}$$

which describes the gain and loss on all the sites ($y = 1$) for $\gamma > 0$ and $\gamma < 0$, respectively. We then calculate the real and imaginary parts of the energy spectrum of the total system $H = H_0 + H_y$ under cylinder geometry, which are respectively shown in Fig. 5a and b. As we see from Fig. 5a and b, two imaginary in-gap states still emerge when the only loss is present, similar to the results for the boundaries with alternating gain and loss. By comparing Fig. 5a and b with Fig. 1b, c, we find that the only slight difference is that the imaginary part of the eigenenergies of the upper chiral edge mode now becomes negative. This does not affect the main conclusions on the imaginary in-gap states and the NHPE.

The general existence of NHPE can be understood in the RG sense. The RG analysis discussed above is general and can be applied to gapped quantum systems with a generic non-Hermitian boundary. For instance, we consider Eq. (18) being added to the QWZ model and perform the real-space RG analysis.

Similar to the RG analysis for the case with alternating loss and gain, the bulk Hamiltonian can be decomposed into different layers coupled via hopping matrix T_y . The key fact here is that the iterative relationship between the effective Hamiltonian of the l th and that of the $(l + 1)$ th layer, i.e., Eq. (11), does not change as long as T_y remains the same. Thus, the effective Hamiltonian for the $(l + 1)$ th layer can still be written as Eq. (4) which leads to the same result as Eq. (15). This indicates that the different non-Hermitian boundary terms only leads to different initial value f_1 , and the RG flow of f_l remains qualitatively the same, independent of f_1 . Consequently, the same fixed point with $\text{Im}[f_l] = 0$ will always be reached for large l . This means that NHPE is general and does not depend on the form of non-Hermitian boundary.

Since the RG analysis shows that the non-Hermitian effect induced by the boundary would always decay and vanish for large distances from the boundary, the effects from different non-Hermitian boundaries would become independent from each other for systems larger than the decay length. Therefore, similar non-Hermitian phenomena are expected if non-Hermitian terms are considered on both the upper and lower boundaries.

To further support the RG results, we also calculate the typical spatial distribution of the imaginary in-gap state under OBCs. As shown in Fig. 5c, corner states still emerge for the gain-only or loss-only boundaries, as a result of the combined effect of the NHPE and NHSE, indicating the general existence of NHPE.

We now show that the NHPE is not only independent of the specific forms of the boundary but is also independent of the specific models of the insulating bulk. Instead of the QWZ model, we now consider a more general 2D two-band model

with a bulk gap m described by the following Hamiltonian:

$$H_0(k_x, k_y) = \sum_{i=x,y} (\cos k_i \sigma_x + \sin k_i \sigma_y) + m \sigma_z, \quad (19)$$

along with the non-Hermitian boundary term $H_y = i \sum_x c_{x,1}^\dagger \gamma \sigma_x c_{x,1}$, i.e., Eq. (3). Then we calculate the energy spectrum under cylinder geometry. Fig. 5d, e show the real and imaginary part of the energy spectrum, which clearly indicate the emergence of the imaginary in-gap states, similar to those for the QWZ model.

As discussed above, the general existence of NHPE can be proved by real-space RG calculations. We, therefore, decompose the total system $H = H_0 + H_y$ (where H_0 is given by Eq. (19) above) into a series of coupled 1D horizontal layers. The Hamiltonian of the $l = 1$ layer reads as $H_{1,k_x} = (\cos k_x + iy) \sigma_x + \sin k_x \sigma_y + m \sigma_z$ and the inter-layer hopping matrix is $T_y = \sigma^+$. Then, we can derive the renormalized Hamiltonian for the $(l + 1)$ th layer by iteratively integrating out the l th layer, leading to:

$$H_{l+1,k_x}^{\text{eff}} = \cos k_x \sigma_x + \sin k_x \sigma_y + m \sigma_z + f_l (\sigma_0 - \sigma_z), \quad (20)$$

where complex self-energy f_l encodes the non-Hermitian effect. Similarly, it can be proved that f_l always saturates to the same fixed point with $\text{Im}[f_l] = 0$ for large l . This clearly suggests the boundary-induced non-Hermitian effect decays and finally vanishes deep in the bulk for large l . Since Eq. (19) is the minimal model of 2D insulators without any specific requirements, the NHPE found here is expected to be a general result for gapped quantum systems with a non-Hermitian boundary. This is also consistent with the emergence of imaginary in-gap states shown in Fig. 5d, e.

In particular, we mention that the NHSE is model-dependent and it does not occur in the above 2D insulator model. However, the NHPE remains intact. Correspondingly, the distribution of the imaginary in-gap state calculated under open boundaries no longer shows up as a corner mode, but is manifested by an edge mode evenly distributed along the upper boundary (Fig. 5f). This indicates that the NHPE could be a more general non-Hermitian effect than the NHSE.

Local density of states of the non-Hermitian vertical chain model. In the Hermitian systems, the DOS can be calculated from the imaginary part of the retarded Green's function $\rho(\epsilon) = -\frac{1}{\pi} \text{Im} \text{Tr} \left[\sum_n \frac{|\psi_n\rangle\langle\psi_n|}{\epsilon + i\eta - E_n} \right]$, where $\eta = 0^+$, $H|\psi_n\rangle = E_n|\psi_n\rangle$, $n = 1, 2, \dots, N$. For the LDOS at the l th site, we have

$$\begin{aligned} \rho_l(\epsilon) &= -\frac{1}{\pi} \text{Im} \left[\sum_n \frac{\langle l|\psi_n\rangle\langle\psi_n|l\rangle}{\epsilon + i\eta - E_n} \right] \\ &= \frac{1}{\pi} \sum_n \frac{\eta \langle l|\psi_n\rangle\langle\psi_n|l\rangle}{(\epsilon - E_n)^2 + \eta^2} \\ &= \sum_n \delta(\epsilon - E_n) |\langle l|\psi_n\rangle|^2. \end{aligned} \quad (21)$$

The last step in the above equation exploits the fact that the Dirac delta function is the limit of the Lorentzian function with η going to zero, and the final result goes back to the definition of the DOS. However, Eq. (21) no longer holds for non-Hermitian Hamiltonians, since E_n is now complex which makes it invalid. Thus, the way to calculate the LDOS has to be generalized to capture the non-Hermitian systems^{59,60}. For a non-Hermitian Hamiltonian, the left or right eigenstates alone do not satisfy the orthogonality condition; both the left and right eigenstates should be used which satisfy the bi-orthogonal relation⁶¹, i.e., $\langle \psi_n^L | \psi_n^R \rangle = \delta_{mn}$, where $H|\psi_n^R\rangle = E_n|\psi_n^R\rangle$, $H^\dagger|\psi_n^L\rangle = E_n^*|\psi_n^L\rangle$, $n = 1, 2, \dots, N$. Incorporating it into Eq. (21), the LDOS at the l th site of the 1D vertical chain model can be expressed as

$$\begin{aligned} \rho_l(\epsilon_r, \epsilon_i) &= \frac{1}{N} \sum_n \delta(\epsilon_r - \text{Re}[E_n]) \delta(\epsilon_i - \text{Im}[E_n]) \\ &\quad \times |\langle l|\psi_n^R\rangle\langle\psi_n^L|l\rangle|, \end{aligned} \quad (22)$$

where $\rho_l(\epsilon_r, \epsilon_i)$ is defined on the complex energy plane, where ϵ_r (ϵ_i) represents the real (imaginary) part of the complex energy ϵ . In our numerical calculations, since the 1D vertical chain model has sublattice degrees of freedom, $N = 2L_y$ with L_y is the 1D chain length, and the phase factor $\langle l|\psi_n^R\rangle\langle\psi_n^L|l\rangle$ includes the sum of the $(2l - 1, 2l - 1)$ and $(2l, 2l)$ matrix elements of the $2L_y \times 2L_y$ matrix. Besides, in the plot of the LDOS, the δ -peaks are broadened by a finite width controlled by a factor b . This is achieved by treating the Dirac- δ function as a Lorentzian form $\delta(\omega - \omega_n) \rightarrow \frac{1}{2\pi} \frac{b}{(\omega - \omega_n)^2 + b^2}$.

Time-evolution of Gaussian wave packet. We set the initial state as a 2D Gaussian wave packet

$$\psi(t=0) = \frac{1}{(4\pi\sigma^2)^{\frac{3}{2}}} \exp \left[-\frac{(x-x_0)^2}{4\sigma^2} - \frac{(y-y_0)^2}{4\sigma^2} \right] (1, 1)^T, \quad (23)$$

where (x_0, y_0) represents the center of the wave packet. According to the Schrödinger equation $i\partial_t|\psi(t)\rangle = H|\psi(t)\rangle$, the time-evolution operator of the

non-Hermitian system is expressed as

$$U(t) = e^{-iHt} = \sum_n e^{-iE_n t} |\psi_n^R\rangle\langle\psi_n^L|, \quad (24)$$

which shows that those modes with $\text{Im}[E_n] < 0$ will vanish due to the exponentially decaying factor, whereas those with $\text{Im}[E_n] > 0$ will dominate in the long-time limit. For the model of the Chern insulator with a non-Hermitian boundary in our work, since the term H_y contains an imaginary unit factor, the total Hamiltonian satisfies $H^*(y) = H_0 - H_y = H_0 + H_{-y} = H(-y)$. So the sign of γ determines the sign of $\text{Im}[E_n]$, which in turn determines whether the mode amplitude grows or decays.

Realization of the non-Hermitian boundaries via coupling to environments. In open quantum systems, the coupling between the system and the environment can be described by the Lindblad master equation, i.e.,

$$\frac{d\rho}{dt} = -i[H, \rho] + \sum_\mu \left(2L_\mu \rho L_\mu^\dagger - \{L_\mu^\dagger L_\mu, \rho\} \right), \quad (25)$$

where ρ is the density matrix, L_μ 's are the Lindblad dissipators describing quantum jumps due to coupling to the environment. The short-time evolution is described by the Schrödinger evolution under the effective non-Hermitian Hamiltonian $H_{\text{eff}} = H - i \sum_\mu L_\mu^\dagger L_\mu$ with $d\rho/dt = -i(H_{\text{eff}}\rho - \rho H_{\text{eff}}^\dagger)$ ^{43,68}. Considering the single particle loss and gain with the loss and gain dissipators:

$$\begin{aligned} L_\mu^l &= \sqrt{\gamma_l} (c_{\mu a} + c_{\mu b}), \\ L_\mu^g &= \sqrt{\gamma_g} (c_{\mu a}^\dagger + c_{\mu b}^\dagger). \end{aligned} \quad (26)$$

Eq. (26) leads to the effective Hamiltonian, which reads in momentum space as

$$H_{\text{eff}} = H + i(\gamma_g - \gamma_l)(\sigma_0 + \sigma_x). \quad (27)$$

The second term in Eq. (27) has a form that produces the non-Hermitian boundary studied in Eq. (3) and Eq. (18). The loss and gain dissipators in Eq. (26) can be realized in reservoir engineering by using nonlocal couplings to auxiliary degrees of freedom which undergo local loss or gain¹¹.

Data availability

The data generated and analyzed during this study are available from the corresponding author upon reasonable request.

Code availability

All codes used to generate the plots within this paper are available from the corresponding author upon reasonable request.

Received: 15 February 2023; Accepted: 21 June 2023;

Published online: 01 July 2023

References

- Breuer, H. P. et al. *The Theory of Open Quantum Systems* (Oxford University Press on Demand, 2002).
- Landi, G. T., Poletti, D. & Schaller, G. Nonequilibrium boundary-driven quantum systems: models, methods, and properties. *Rev. Mod. Phys.* **94**, 045006 (2022).
- Carmichael, H. *An Open Systems Approach to Quantum Optics* (Springer Science & Business Media, 2009).
- Rotter, I. A non-Hermitian Hamilton operator and the physics of open quantum systems. *J. Phys. A* **42**, 153001 (2009).
- Bender, C. M. & Boettcher, S. Real spectra in non-Hermitian Hamiltonians having PT symmetry. *Phys. Rev. Lett.* **80**, 5243 (1998).
- Esaki, K., Sato, M., Hasebe, K. & Kohmoto, M. Edge states and topological phases in non-Hermitian systems. *Phys. Rev. B* **84**, 205128 (2011).
- Lee, T. E. Anomalous edge state in a non-Hermitian lattice. *Phys. Rev. Lett.* **116**, 133903 (2016).
- Yao, S., Song, F. & Wang, Z. Non-Hermitian Chern bands. *Phys. Rev. Lett.* **121**, 136802 (2018).
- Kunst, F. K., Edvardsson, E., Budich, J. C. & Bergholtz, E. J. Biorthogonal bulk-boundary correspondence in non-Hermitian systems. *Phys. Rev. Lett.* **121**, 026808 (2018).
- Kawabata, K., Shiozaki, K. & Ueda, M. Anomalous helical edge states in a non-Hermitian Chern insulator. *Phys. Rev. B* **98**, 165148 (2018).
- Gong, Z., Ashida, Y., Kawabata, K., Takasan, K., Higashikawa, S. & Ueda, M. Topological phases of non-Hermitian systems. *Phys. Rev. X* **8**, 031079 (2018).

12. Lee, J. Y., Ahn, J., Zhou, H. & Vishwanath, A. Topological correspondence between Hermitian and non-Hermitian systems: anomalous dynamics. *Phys. Rev. Lett.* **123**, 206404 (2019).
13. Wang, H., Ruan, J. & Zhang, H. Non-Hermitian nodal-line semimetals with an anomalous bulk-boundary correspondence. *Phys. Rev. B* **99**, 075130 (2019).
14. Kawabata, K., Shiozaki, K., Ueda, M. & Sato, M. Symmetry and topology in non-Hermitian physics. *Phys. Rev. X* **9**, 041015 (2019).
15. Luo, X. W. & Zhang, C. Higher-order topological corner states induced by gain and loss. *Phys. Rev. Lett.* **123**, 073601 (2019).
16. Zhang, K., Yang, Z. & Fang, C. Correspondence between winding numbers and skin modes in non-Hermitian systems. *Phys. Rev. Lett.* **125**, 126402 (2020).
17. Roccati, F. et al. Hermitian and non-Hermitian topology from photon-mediated interactions. Preprint at *arXiv* <https://doi.org/10.48550/arXiv.2303.00762>.
18. Yao, S. & Wang, Z. Edge states and topological invariants of non-Hermitian systems. *Phys. Rev. Lett.* **121**, 086803 (2018).
19. Lee, C. H. & Thomale, R. Anatomy of skin modes and topology in non-Hermitian systems. *Phys. Rev. B* **99**, 201103 (2019).
20. Lee, C. H., Li, L. & Gong, J. Hybrid higher-order skin-topological modes in nonreciprocal systems. *Phys. Rev. Lett.* **123**, 016805 (2019).
21. Longhi, S. Probing non-Hermitian skin effect and non-Bloch phase transitions. *Phys. Rev. Res.* **1**, 023013 (2019).
22. Okuma, N., Kawabata, K., Shiozaki, K. & Sato, M. Topological origin of non-Hermitian skin effects. *Phys. Rev. Lett.* **124**, 086801 (2020).
23. Yi, Y. & Yang, Z. Non-Hermitian skin modes induced by on-site dissipations and chiral tunneling effect. *Phys. Rev. Lett.* **125**, 186802 (2020).
24. Kawabata, K., Sato, M. & Shiozaki, K. Higher-order non-Hermitian skin effect. *Phys. Rev. B* **102**, 205118 (2020).
25. Okuma, N. & Sato, M. Non-Hermitian skin effects in hermitian correlated or disordered systems: quantities sensitive or insensitive to boundary effects and pseudo-quantum-number. *Phys. Rev. Lett.* **126**, 176601 (2021).
26. Sun, X. Q., Zhu, P. & Hughes, T. L. Geometric response and disclination-induced skin effects in non-Hermitian systems. *Phys. Rev. Lett.* **127**, 066401 (2021).
27. Li, Y., Liang, C., Wang, C., Lu, C. & Liu, Y. C. Gain-loss-induced hybrid skin-topological effect. *Phys. Rev. Lett.* **128**, 223903 (2022).
28. Zhang, X. et al. A review on non-Hermitian skin effect. *Adv. Phys. X* **7**, 2109431 (2022).
29. Roccati, F. Non-Hermitian skin effect as an impurity problem. *Phys. Rev. A* **104**, 022215 (2021).
30. Shen, H., Zhen, B. & Fu, L. Topological band theory for non-Hermitian Hamiltonians. *Phys. Rev. Lett.* **120**, 146402 (2018).
31. Zhou, H., Peng, C., Yoon, Y., Hsu, C. W., Nelson, K. A., Fu, L., Joannopoulos, J. D., Soljačić, M. & Zhen, B. Observation of bulk Fermi arc and polarization half charge from paired exceptional points. *Science* **359**, 1009 (2018).
32. Yin, C., Jiang, H., Li, L., Lü, R. & Chen, S. Geometrical meaning of winding number and its characterization of topological phases in one-dimensional chiral non-Hermitian systems. *Phys. Rev. A* **97**, 052115 (2018).
33. Yokomizo, K. & Murakami, S. Non-Bloch band theory of non-hermitian systems. *Phys. Rev. Lett.* **123**, 066404 (2019).
34. Song, F., Yao, S. & Wang, Z. Non-Hermitian topological invariants in real space. *Phys. Rev. Lett.* **123**, 246801 (2019).
35. Deng, T.-S. & Yi, W. Non-Bloch topological invariants in a non-Hermitian domain wall system. *Phys. Rev. B* **100**, 035102 (2019).
36. K. Kawabata, N. O. & Sato, M. Non-Bloch band theory of non-Hermitian Hamiltonians in the symplectic class. *Phys. Rev. B* **101**, 195147 (2020).
37. Yang, Z., Zhang, K., Fang, C. & Hu, J. Non-Hermitian bulk-boundary correspondence and auxiliary generalized Brillouin zone theory. *Phys. Rev. Lett.* **125**, 226402 (2020).
38. Kawabata, K., Shiozaki, K. & Ryu, S. Topological field theory of non-hermitian systems. *Phys. Rev. Lett.* **126**, 216405 (2021).
39. Xue, W. T., Li, M. R., Hu, Y. M., Song, F. & Wang, Z. Simple formulas of directional amplification from non-Bloch band theory. *Phys. Rev. B* **103**, L241408 (2021).
40. Wu, D., Xie, J., Zhou, Y. & An, J. Connections between the open-boundary spectrum and the generalized Brillouin zone in non-Hermitian systems. *Phys. Rev. B* **105**, 045422 (2022).
41. Rui, W. B., Zheng, Z., Wang, C. & Wang, Z. D. Non-Hermitian spatial symmetries and their stabilized normal and exceptional topological semimetals. *Phys. Rev. Lett.* **128**, 226401 (2022).
42. Yoshida, T., Peters, R. & Kawakami, N. Non-Hermitian perspective of the band structure in heavy-fermion systems. *Phys. Rev. B* **98**, 035141 (2018).
43. Song, F., Yao, S. & Wang, Z. Non-Hermitian skin effect and chiral damping in open quantum systems. *Phys. Rev. Lett.* **123**, 170401 (2019).
44. Zhou, B., Wang, R. & Wang, B. Renormalization group approach to non-Hermitian topological quantum criticality. *Phys. Rev. B* **102**, 205116 (2020).
45. Meissner, H. Superconductivity of contacts with interposed barriers. *Phys. Rev.* **117**, 672 (1960).
46. Liu, X., Wang, Z., Xie, X. C. & Yu, Y. Abelian and non-Abelian anyons in integer quantum anomalous Hall effect and topological phase transitions via superconducting proximity effect. *Phys. Rev. B* **83**, 125105 (2011).
47. Xu, J. P. et al. Artificial topological superconductor by the proximity effect. *Phys. Rev. Lett.* **112**, 217001 (2014).
48. Zhu, G. Y., Zhang, F. C. & Zhang, G. M. Proximity-induced superconductivity in monolayer CuO_2 on cuprate substrates. *Phys. Rev. B* **94**, 174501 (2016).
49. Yu, L. Bound state in superconductors with paramagnetic impurities. *Acta Phys. Sin.* **21**, 75 (1965).
50. Shiba, H. Classical spins in superconductors. *Prog. Theor. Phys.* **40**, 435 (1968).
51. Rusinov, A. I. Superconductivity near a paramagnetic impurity. *JETP Lett.* **9**, 85 (1969).
52. Wang, W., Qin, S., Lu, Z. Y., Yu, L. & Su, Z. Impurity energy level in the Haldane gap. *Phys. Rev. B* **53**, 40 (1996).
53. Hyman, R. A. & Yang, K. Impurity driven phase transition in the antiferromagnetic spin-1 chain. *Phys. Rev. Lett.* **78**, 1783 (1997).
54. Balatsky, A. V., Vekhter, I. & Zhu, J. X. Impurity-induced states in conventional and unconventional superconductors. *Rev. Mod. Phys.* **78**, 373 (2006).
55. Yin, J. X. et al. Observation of a robust zero-energy bound state in iron-based superconductor $\text{Fe}(\text{Te},\text{Se})$. *Nat. Phys.* **11**, 543 (2015).
56. Zheng, S. H. et al. Interplay of quantum impurities and topological surface modes. *Phys. Lett. A* **379**, 2890 (2015).
57. Sun, H. H. et al. Majorana zero mode detected with spin selective Andreev reflection in the vortex of a topological superconductor. *Phys. Rev. Lett.* **116**, 257003 (2016).
58. Qi, X. L., Wu, Y. S. & Zhang, S. C. Topological quantization of the spin Hall effect in two-dimensional paramagnetic semiconductors. *Phys. Rev. B* **74**, 085308 (2006).
59. Brouwer, P., Silvestrov, P. & Beenakker, C. Theory of directed localization in one dimension. *Phys. Rev. B* **56**, R4333 (1997).
60. Mudry, C., Brouwer, P., Halperin, B., Gurarie, V. & Zee, A. Density of states in the non-Hermitian Lloyd model. *Phys. Rev. B* **58**, 13539 (1998).
61. Brody, D. C. Biorthogonal quantum mechanics. *J. Phys. A* **47**, 035305 (2013).
62. Sukhachov, P. O. & Balatsky, A. V. Non-Hermitian impurities in Dirac systems. *Phys. Rev. Res.* **2**, 013325 (2020).
63. Li, L., Lee, C. H. & Gong, J. Impurity induced scale-free localization. *Commun. Phys.* **4**, 1 (2021).
64. Yu, R. et al. Quantized anomalous Hall effect in magnetic topological insulators. *Science* **329**, 61 (2010).
65. Reiter, F. & Sørensen, A. S. Effective operator formalism for open quantum systems. *Phys. Rev. A* **85**, 032111 (2012).
66. Zhao, H. et al. Topological hybrid silicon microlasers. *Nat. Commun.* **9**, 981 (2018).
67. Mittal, S. et al. Photonic quadrupole topological phases. *Nat. Photonics* **13**, 692 (2019).
68. Nakagawa, M., Kawakami, N. & Ueda, M. Non-Hermitian Kondo effect in ultracold alkaline-earth atoms. *Phys. Rev. Lett.* **121**, 203001 (2018).

Acknowledgements

This work was supported by the National Natural Science Foundation of China (Grant nos. 12274206, 12034014, and 11904245), the Innovation Program for Quantum Science and Technology (Grant no. 2021ZD0302800), National Key R&D Program of China (Grant no. 2022YFA1403601), and the Xiaomi foundation.

Author contributions

R.W., B.W., and D.Y.X. conceived the project. D.W. developed the theoretical model. D.W. and J.C. performed the calculations supervised by R.W. W.S. performed the numerical renormalization group calculations of the impurity model. R.W. and D.W. co-wrote the paper with input from other authors. All authors discussed the results.

Competing interests

The authors declare no competing interests.

Additional information

Supplementary information The online version contains supplementary material available at <https://doi.org/10.1038/s42005-023-01282-1>.

Correspondence and requests for materials should be addressed to Rui Wang.

Peer review information *Communications Physics* thanks the anonymous reviewers for their contribution to the peer review of this work. A peer review file is available.

Reprints and permission information is available at <http://www.nature.com/reprints>

Publisher's note Springer Nature remains neutral with regard to jurisdictional claims in published maps and institutional affiliations.



Open Access This article is licensed under a Creative Commons Attribution 4.0 International License, which permits use, sharing, adaptation, distribution and reproduction in any medium or format, as long as you give appropriate credit to the original author(s) and the source, provide a link to the Creative Commons license, and indicate if changes were made. The images or other third party material in this article are included in the article's Creative Commons license, unless indicated otherwise in a credit line to the material. If material is not included in the article's Creative Commons license and your intended use is not permitted by statutory regulation or exceeds the permitted use, you will need to obtain permission directly from the copyright holder. To view a copy of this license, visit <http://creativecommons.org/licenses/by/4.0/>.

© The Author(s) 2023